Platinum substrate for surface plasmon microscopy at small angles

Hossein Hassani[1,2], Nikolaus Radja Wolf[1], Xiaobo Yuan[1], Roger Wördenweber[1], and Andreas Offenhäusser[1,2,*]

[1]*Forschungszentrum Jülich GmbH, Institute of Biological Information Processing, Bioelectronics (IBI-3), Jülich, Germany*
[2]*RWTH Aachen University, I. Institute of Physics (IA), Aachen, Germany*
**Corresponding author: a.offenhaeusser@fz-juelich.de*

Received XX Month XXXX; revised XX Month, XXXX; accepted XX Month XXXX; posted XX Month XXXX (Doc. ID XXXXX); published XX Month XXXX

Platinum is reported as the main component of the substrate in surface plasmon microscopy of metal–dielectric interface for small-angle measurements. In the absence of a narrow dip in the angular spectrum of platinum, the refractive index of the dielectric medium or the thickness of a deposited layer is proven deducible from the observed sharp peak, close to the critical angle. The sensitivities of refractive index and thickness measurements using platinum are compared with that of a gold surface plasmon resonance chip. Furthermore, the thickness of a structured layer of (3-Aminopropyl)triethoxysilane on the platinum substrate is measured to be 0.7 nm, demonstrating high sensitivity of the technique.

http://dx.doi.org/10.1364/OL.99.099999

Over the past few decades, surface plasmon resonance (SPR) microscopy has become a well-established technique to investigate metal–dielectric interface in a variety of contexts. It was initially noted as a capable tool to image low-contrast features on metal films [1–3]. Later, several groups applied this tool to cell–metal interface to image adherent living cells [4–9]. Due to its remarkable sensitivity to the vertical distribution of the refractive index (RI) within a sub-wavelength distance from the interface, SPR microscopy has become a standard technique to map cell–metal distance [10–15] and intracellular refractive index (RI) [15–17].

Being noble, biocompatible and highly conductive, as well as demonstrating resonance in the supercritical part of the reflectance spectrum, has rendered gold the standard choice for SPR techniques. Moreover, the availability and ease of fabrication with gold has enabled researchers to benefit from this sensitive technique especially in biosensing applications. Nevertheless, most surface plasmon microscopy (SPM) setups rely on objective-based illumination of the sample at large angles, which requires high numerical aperture objectives, and therefore high-end optical setups. To reduce this barrier, alternative substrates with well-defined features in their reflectance spectrum at smaller angles are preferred. Moreover, such features must exhibit high sensitivity to the optical properties of the dielectric medium.

Platinum is another noble metal with a broad use in industry and research, such as in jewelry, fuel cells, hydrogen storage, chemical sensors and biosensors. It has also been reported as an additional coating layer for silver SPR biosensors to provide a better chemical resistance and higher sensitivity [18]. Yet, due to the lack of a narrow resonance dip in its angular spectrum of reflectance, platinum has not been considered as the main element of the substrate in SPM. Here we report platinum-based SPM that, instead of resonance, relies on a peak in the close proximity of the critical angle.

Table 1. The multilayer structure of the substrate

Layer	Refractive Index	Thickness [nm]
Glass	1.788	∞
Ti	$3.3 + i\,3.8$	6
Pt	$2.8 + i\,5.6$	17
Medium (Air)	1.000	∞

A high-index coverslip is coated with 6 and 17 nm of titanium and platinum, respectively. Titanium serves as an adhesion layer. Since the metallization parameters such as base pressure of the evaporator and the deposition rate can alter the optical properties of the resulting films [19], there are several values reported for the refractive indices of titanium [20,21] and platinum [22,23]. Hence, as the initial step of data analysis, we employ the Fresnel equations and transfer-matrix method to numerically fit a layer structure model to the reflectance data of the bare substrate [Fig. 1] in order to specifically determine the thickness and the complex RI of our metal layers [Table 1]. As seen in Fig. 1, this approach provides us with a layer model that fits the data over a broad range of angles.

Although substrates with different values of thickness of metal layers are expected to lead to qualitatively similar results, in the following we limit our calculations to the fabricated sample according to Table 1, in order to provide a numerical characterization of the substrate that matches our measurement.

According to calculated reflectance curves based on the layer model of Table 1, with the RI of the medium varying in the range of 1–1.5 *RIU* (refractive index unit), the peak angle of the platinum substrate spans 34–58°. For comparison with a gold SPR chip, we substitute the platinum layer in Table 1 with 45 *nm* of gold (RI_{gold} = 0.18 + *i* 3.43 [24]) and calculate the resonance angle [Fig. 1] for different values of the RI of the medium. According to Fig. 2(a), the resonance angle of the gold substrate varies in the range of 36–67°.

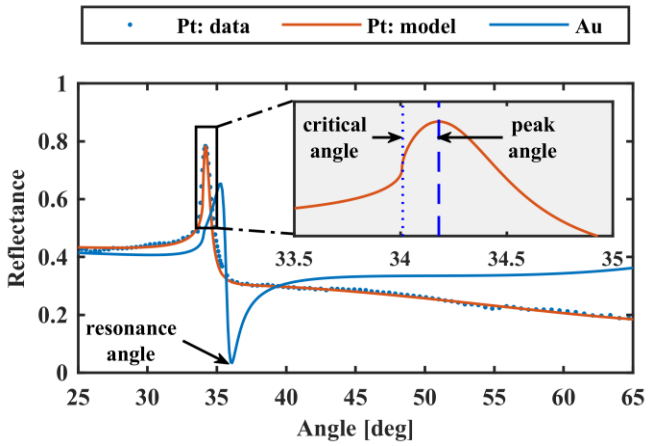

Fig. 1. Model and data of reflectance vs. angle for a sample consisting of glass/Ti/Pt/air and alternatively SPR on a gold substrate. The inset shows a magnified view of the peak region of the model for Pt substrate, containing both critical angle and peak angle. The parameters of the Pt substrate are taken from Table 1.

The sensitivities of the peak angle in the platinum substrate and the resonance angle in the gold substrate upon changes in the RI of the medium are defined as $|\partial\theta_{peak}/\partial RI_{medium}|$ and $|\partial\theta_{resonance}/\partial RI_{medium}|$, respectively. The gold SPR chip offers a 1.2–2-fold higher RI sensitivity over this range [Fig. 2(b)].

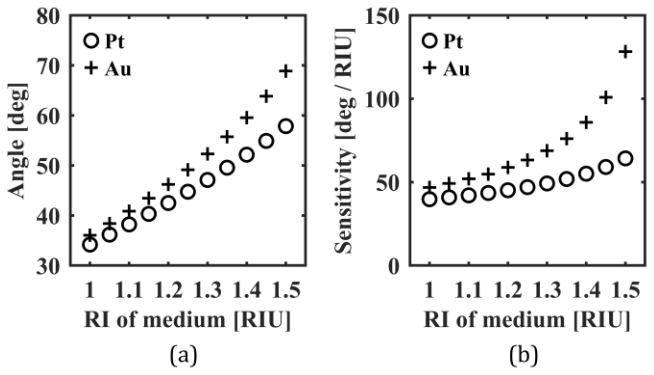

Fig. 2: (a) Peak angle of the platinum substrate and resonance angle of the gold substrate vs. RI of the medium, and (b) sensitivities of the two angles upon changes in the RI.

(3-Aminopropyl)triethoxysilane (APTES) is a widely applied coupling agent to prepare amine-terminated films [25–29]. It is frequently used for biosensing applications since it allows to covalently bind proteins and other organic macromolecules to inorganic surfaces. According to Cauchy's formula, the refractive index of APTES at the wavelength of the laser is 1.429 [30].

Table 2. The multilayer structure of the APTES sample

Layer	Refractive Index	Thickness [nm]
Glass	1.788	∞
Ti	3.3 + *i* 3.8	6
Pt	2.8 + *i* 5.6	17
APTES	1.429	?
Air	1.000	∞

In order to measure the thickness of a layer of APTES on the platinum substrate we first show the dependence of the peak angle on the thickness of the layer through the calculation of reflectance for a series of layer structures according to Table 2. In these calculations, the thickness of APTES is varied in the range of 0–10 *nm*. Consequently, as shown in Fig. 3(a), the peak angle covers an angular range of 34.19–34.43°. The resonance angle of the equivalent gold substrate for the same range of APTES thickness changes within 36.1–37°. Similar to the previous case, the sensitivities of the two variables with respect to the thickness of the APTES layer are calculated and shown in Fig. 3(b), demonstrating about 4-fold higher thickness sensitivity of peak angle of the gold substrate.

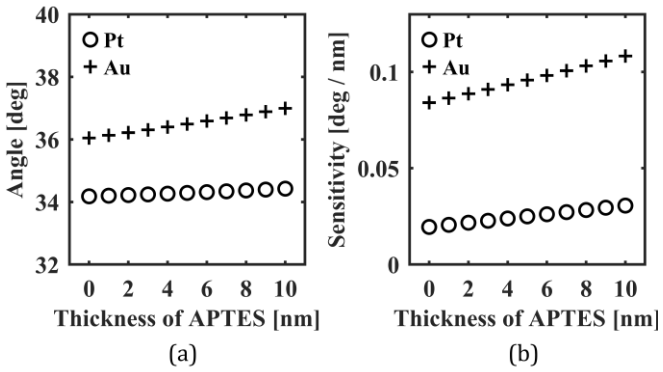

Fig. 3: (a) Peak angle of platinum substrates and resonance angle of gold substrates vs. thickness of an additional APTES layer, and (b) resulting sensitivities of the two angles upon changes in the thickness of the APTES layer.

In order to apply these calculations to a real sample, a platinum substrate with a patterned APTES layer is fabricated according to Table 2 at Helmholtz Nano Facility. A high refractive index coverslip (Olympus, HIGHINDEX-CG) is coated with titanium and platinum layers. Using electron beam lithography and lift-off technique, gas-phase-deposited APTES [29] is patterned on platinum in form of multiple parallel APTES stripes with a width of 12.5 μm and a spacing of 12.5 μm between the stripes. The thickness of APTES remains unknown. The substrate is then inserted into the SPM setup using a high-RI immersion oil (RI = 1.78, Cargille Laboratories).

In the optical setup, a 632.8 *nm* He-Ne laser beam is transmitted through a rotating ground glass, collected and collimated, radially polarized (ZPol, Nanophoton Corp.), and coupled into the back focal

plane (BFP) of an objective lens (Apo N 100× HOTIRF, Olympus) with *NA* = 1.7, granting a broad illumination cone. The beam is focused on the sample, reflected from it, and collected with the objective lens. Finally, the BFP of the objective is captured with a CMOS camera to record the reflectance at the position of the beam on the sample. A motorized XY stage (M-687.UL, Physik Instrumente GmbH & Co.) assists with the scanning over the sample.

Each angular intensity profile, $I(\theta)$, is extracted from the radial profile of a BFP image, according to Abbe sine condition. To calculate the reflectance profile, $R(\theta)$, the intensity profile of the sample is divided by the intensity profile of a custom-made silver mirror (reflectance ≥ 98%). To achieve a sub-pixel accuracy in determining the peak angle, we fit a parabola to the tip of the peak in the reflectance profile and define the corresponding angle to its vertex as the peak angle [31].

Based on Fig. 3(a), the thickness values are assigned to each scan point and the thickness map is formed accordingly [Fig. 4(a)]. The average of the map along the APTES stripes provides us with the mean cross-section of the patterned APTES layer on platinum [Fig. 4(b)], demonstrating the expected width and spacing of the APTES stripes as well as an average peak-to-valley value of 0.7 ± 0.1 *nm*, suggesting the formation of a monolayer of APTES on the platinum substrate [25,30,32].

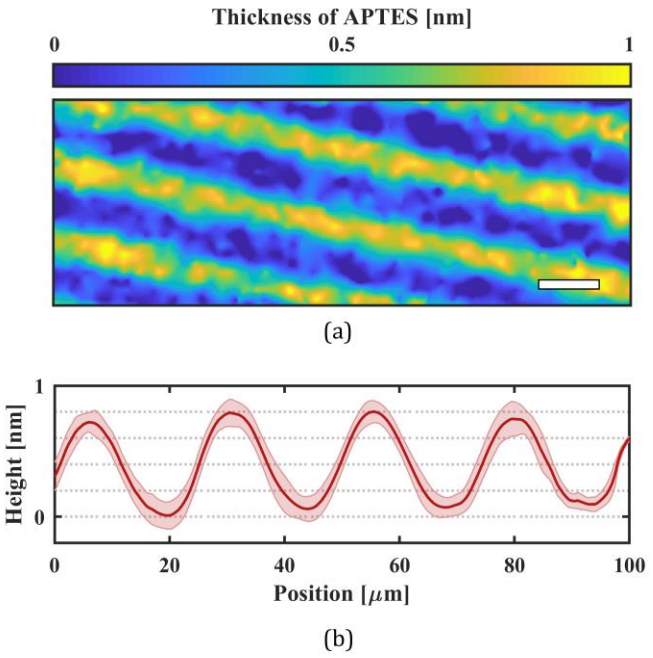

Fig. 4: (a) Thickness map of APTES stripes on a platinum substrate shows the expected structure. The scale bar is 20 μm. Mean and standard deviation over the whole map is calculated along the stripes, to demonstrate (b) average and error of the cross-section of the structure with an average peak-to-valley value of 0.7 ± 0.1 *nm*.

In Principle, the performed calculations and measurements can be done based on a coverslip with lower RI, such as BK-7. Alternatively, one can utilize Snell's law to directly translate our reported angular values to the corresponding values on any alternative coverslip.

According to Fig. 1, peak angle can be defined for gold substrate as well. Since it occurs at an angle larger than the peak angle of platinum substrate, platinum remains the better choice if the goal is to achieve a smaller angle of observation or consequently a broader RI range. Furthermore, to compare the vulnerabilities of these features to spatial noise of the optical signal, the second derivative of reflectance is a relevant quantity. For instance in Fig. 1 the second derivatives of the reflectance curves at the peak angle of platinum, the peak angle of gold and the resonance angle of gold are -7.0, -1.8 and 2.3 [$1/deg^2$] respectively. Hence, the peak angle of platinum is about 4 and 3 times sharper than the peak angle and the resonance angle of gold, respectively. At larger RI values of medium, all these extrema become broader.

In this work we investigated a novel layer structure for SPM, which not only allows us to study different surface processes on platinum, but also makes the measurement accessible to a broader range of RI values. Moreover, if the numerical aperture of the objective lens sets a limit to the feasibility of a measurement, the introduced substrate might provide a solution. The platinum substrate shows a lower sensitivity to the RI of the medium and the thickness of a coating layer. Nevertheless, the sharpness of the reflectance curve at the peak angle provides us with the high accuracy which is for instance necessary for the measurement of a sub-nanometer thick molecular layer like an APTES monolayer. This measurement principle is applicable to any other substrate that exhibits a peak in the super-critical angle region of its reflectance.

Funding. Helmholtz Association.

Disclosures. The authors declare no conflicts of interest.

References

1. E. Yeatman and E. a. A. Ash, Electron. Lett. **23**, 1091 (1987).
2. B. Rothenhäusler and W. Knoll, Nature **332**, 615 (1988).
3. W. Hickel, D. Kamp, and W. Knoll, Nature **339**, 186 (1989).
4. R.-Y. He, C.-Y. Lin, Y.-D. Su, K.-C. Chiu, N.-S. Chang, H.-L. Wu, and S.-J. Chen, Opt. Express **18**, 3649 (2010).
5. A. W. Peterson, M. Halter, A. Tona, K. Bhadriraju, and A. L. Plant, Cytom. Part A **77**, 895 (2010).
6. A. W. Peterson, M. Halter, A. Tona, and A. L. Plant, BMC Cell Biol. **15**, 35 (2014).
7. L. Berguiga, L. Streppa, E. Boyer-Provera, C. Martinez-Torres, L. Schaeffer, J. Elezgaray, A. Arneodo, and F. Argoul, Appl. Opt. **55**, 1216 (2016).
8. Y. Yang, H. Yu, X. Shan, W. Wang, X. Liu, S. Wang, and N. Tao, Small **11**, 2878 (2015).
9. T. Son, C. Lee, J. Seo, I.-H. Choi, and D. Kim, Opt. Lett. **43**, 959 (2018).
10. K. F. Giebel, C. Bechinger, S. Herminghaus, M. Riedel, P. Leiderer, U. Weiland, and M. Bastmeyer, Biophys. J. **76**, 509 (1999).
11. W. Wang, S. Wang, Q. Liu, J. Wu, and N. Tao, Langmuir **28**, 13373 (2012).
12. K. Toma, H. Kano, and A. Offenhäusser, ACS Nano **8**, 12612 (2014).
13. T. Son, J. Seo, I. H. Choi, and D. Kim, Opt. Commun. **422**, 64 (2018).
14. E. Kreysing, S. Seyock, H. Hassani, E. Brauweiler-Reuters, E. Neumann, and A. Offenhäusser, Adv. Mater. Interfaces **7**, 2070026 (2020).
15. E. Kreysing, H. Hassani, N. Hampe, and A. Offenhäusser, ACS Nano **12**, 8934 (2018).
16. K. J. Moh, X.-C. Yuan, J. Bu, S. W. Zhu, and B. Z. Gao, Opt. Express

16, 20734 (2008).
17. H. Hassani and E. Kreysing, Opt. Lett. **44**, 1359 (2019).
18. S. Shukla, M. Rani, N. K. Sharma, and V. Sajal, Optik (Stuttg). **126**, 4636 (2015).
19. K. M. McPeak, S. V. Jayanti, S. J. P. Kress, S. Meyer, S. Iotti, A. Rossinelli, and D. J. Norris, ACS Photonics **2**, 326 (2015).
20. P. B. Johnson and R. W. Christy, Phys. Rev. B **9**, 5056 (1974).
21. K. J. Palm, J. B. Murray, T. C. Narayan, and J. N. Munday, ACS Photonics **5**, 4677 (2018).
22. A. D. Rakić, A. B. Djurišić, J. M. Elazar, and M. L. Majewski, Appl. Opt. **37**, 5271 (1998).
23. W. S. M. Werner, K. Glantschnig, and C. Ambrosch-Draxl, J. Phys. Chem. Ref. Data **38**, 1013 (2009).
24. P. B. Johnson and R. W. Christy, Phys. Rev. B **6**, 4370 (1972).
25. J. A. Howarter and J. P. Youngblood, Langmuir **22**, 11142 (2006).
26. E. A. Smith and W. Chen, Langmuir **24**, 12405 (2008).
27. N. A. Lapin and Y. J. Chabal, J. Phys. Chem. B **113**, 8776 (2009).
28. A. Markov, N. Wolf, X. Yuan, D. Mayer, V. Maybeck, A. Offenhäusser, and R. Wördenweber, ACS Appl. Mater. Interfaces **9**, 29265 (2017).
29. X. Yuan, N. Wolf, D. Mayer, A. Offenhäusser, and R. Wördenweber, Langmuir **35**, 8183 (2019).
30. B. Yameen, C. Rodriguez-Emmenegger, C. M. Preuss, O. Pop-Georgievski, E. Verveniotis, V. Trouillet, B. Rezek, and C. Barner-Kowollik, Chem. Commun. **49**, 8623 (2013).
31. D. G. Bailey, in *Proceeding of Image and Vision Computing New Zealand* (2003), p. 414.
32. E. T. Vandenberg, L. Bertilsson, B. Liedberg, K. Uvdal, R. Erlandsson, H. Elwing, and I. Lundström, J. Colloid Interface Sci. **147**, 103 (1991).

Full References (For review only)

1. E. Yeatman and E. a. A. Ash, "Surface plasmon microscopy," Electron. Lett. **23**, 1091–1092 (1987).
2. B. Rothenhäusler and W. Knoll, "Surface-plasmon microscopy," Nature **332**, 615–617 (1988).
3. W. Hickel, D. Kamp, and W. Knoll, "Surface-plasmon microscopy," Nature **339**, 186 (1989).
4. R.-Y. He, C.-Y. Lin, Y.-D. Su, K.-C. Chiu, N.-S. Chang, H.-L. Wu, and S.-J. Chen, "Imaging live cell membranes via surface plasmon-enhanced fluorescence and phase microscopy," Opt. Express **18**, 3649–3659 (2010).
5. A. W. Peterson, M. Halter, A. Tona, K. Bhadriraju, and A. L. Plant, "Using surface plasmon resonance imaging to probe dynamic interactions between cells and extracellular matrix," Cytom. Part A **77**, 895–903 (2010).
6. A. W. Peterson, M. Halter, A. Tona, and A. L. Plant, "High resolution surface plasmon resonance imaging for single cells.," BMC Cell Biol. **15**, 35 (2014).
7. L. Berguiga, L. Streppa, E. Boyer-Provera, C. Martinez-Torres, L. Schaeffer, J. Elezgaray, A. Arneodo, and F. Argoul, "Time-lapse scanning surface plasmon microscopy of living adherent cells with a radially polarized beam," Appl. Opt. **55**, 1216 (2016).
8. Y. Yang, H. Yu, X. Shan, W. Wang, X. Liu, S. Wang, and N. Tao, "Label-Free Tracking of Single Organelle Transportation in Cells with Nanometer Precision Using a Plasmonic Imaging Technique," Small **11**, 2878–2884 (2015).
9. T. Son, C. Lee, J. Seo, I.-H. Choi, and D. Kim, "Surface plasmon microscopy by spatial light switching for label-free imaging with enhanced resolution," Opt. Lett. **43**, 959 (2018).
10. K. F. Giebel, C. Bechinger, S. Herminghaus, M. Riedel, P. Leiderer, U. Weiland, and M. Bastmeyer, "Imaging of cell/substrate contacts of living cells with surface plasmon resonance microscopy," Biophys. J. **76**, 509–516 (1999).
11. W. Wang, S. Wang, Q. Liu, J. Wu, and N. Tao, "Mapping Single-Cell–Substrate Interactions by Surface Plasmon Resonance Microscopy," Langmuir **28**, 13373–13379 (2012).
12. K. Toma, H. Kano, and A. Offenhäusser, "Label-free measurement of cell-electrode cleft gap distance with high spatial resolution surface plasmon microscopy," ACS Nano **8**, 12612–12619 (2014).
13. T. Son, J. Seo, I. H. Choi, and D. Kim, "Label-free quantification of cell-to-substrate separation by surface plasmon resonance microscopy," Opt. Commun. **422**, 64–68 (2018).
14. E. Kreysing, S. Seyock, H. Hassani, E. Brauweiler-Reuters, E. Neumann, and A. Offenhäusser, "Surface Plasmon Resonance Microscopy: Correlating Surface Plasmon Resonance Microscopy of Living and Fixated Cells with Electron Microscopy Allows for Investigation of Potential Preparation Artifacts (Adv. Mater. Interfaces 6/2020)," Adv. Mater. Interfaces **7**, 2070026 (2020).
15. E. Kreysing, H. Hassani, N. Hampe, and A. Offenhäusser, "Nanometer-Resolved Mapping of Cell-Substrate Distances of Contracting Cardiomyocytes Using Surface Plasmon Resonance Microscopy," ACS Nano **12**, 8934–8942 (2018).
16. K. J. Moh, X.-C. Yuan, J. Bu, S. W. Zhu, and B. Z. Gao, "Surface plasmon resonance imaging of cell-substrate contacts with radially polarized beams," Opt. Express **16**, 20734 (2008).
17. H. Hassani and E. Kreysing, "Noninvasive measurement of the refractive index of cell organelles using surface plasmon resonance microscopy," Opt. Lett. **44**, 1359 (2019).
18. S. Shukla, M. Rani, N. K. Sharma, and V. Sajal, "Sensitivity enhancement of a surface plasmon resonance based fiber optic sensor utilizing platinum layer," Optik (Stuttg). **126**, 4636–4639 (2015).
19. K. M. McPeak, S. V. Jayanti, S. J. P. Kress, S. Meyer, S. Iotti, A. Rossinelli, and D. J. Norris, "Plasmonic films can easily be better: Rules and recipes," ACS Photonics **2**, 326–333 (2015).
20. P. B. Johnson and R. W. Christy, "Optical constants of transition metals: Ti, V, Cr, Mn, Fe, Co, Ni, and Pd," Phys. Rev. B **9**, 5056–5070 (1974).
21. K. J. Palm, J. B. Murray, T. C. Narayan, and J. N. Munday, "Dynamic Optical Properties of Metal Hydrides," ACS Photonics **5**, 4677–4686 (2018).
22. A. D. Rakić, A. B. Djurišić, J. M. Elazar, and M. L. Majewski, "Optical properties of metallic films for vertical-cavity optoelectronic devices," Appl. Opt. **37**, 5271 (1998).
23. W. S. M. Werner, K. Glantschnig, and C. Ambrosch-Draxl, "Optical constants and inelastic electron-scattering data for 17 elemental metals," J. Phys. Chem. Ref. Data **38**, 1013–1092 (2009).
24. P. B. Johnson and R. W. Christy, "Optical constants of the noble metals," Phys. Rev. B **6**, 4370–4379 (1972).
25. J. A. Howarter and J. P. Youngblood, "Optimization of silica silanization by 3-aminopropyltriethoxysilane," Langmuir **22**, 11142–11147 (2006).
26. E. A. Smith and W. Chen, "How to prevent the loss of surface functionality derived from aminosilanes," Langmuir **24**, 12405–12409 (2008).
27. N. A. Lapin and Y. J. Chabal, "Infrared characterization of biotinylated silicon oxide surfaces, surface stability, and specific attachment of streptavidin," J. Phys. Chem. B **113**, 8776–8783 (2009).
28. A. Markov, N. Wolf, X. Yuan, D. Mayer, V. Maybeck, A. Offenhäusser, and R. Wördenweber, "Controlled Engineering of Oxide Surfaces for Bioelectronics Applications Using Organic Mixed Monolayers," ACS Appl. Mater. Interfaces **9**, 29265–29272 (2017).
29. X. Yuan, N. Wolf, D. Mayer, A. Offenhäusser, and R. Wördenweber, "Vapor-Phase Deposition and Electronic Characterization of 3-Aminopropyltriethoxysilane Self-Assembled Monolayers on Silicon Dioxide," Langmuir **35**, 8183–8190 (2019).
30. B. Yameen, C. Rodriguez-Emmenegger, C. M. Preuss, O. Pop-Georgievski, E. Verveniotis, V. Trouillet, B. Rezek, and C. Barner-Kowollik, "A facile avenue to conductive polymer brushes via cyclopentadiene-maleimide Diels-Alder ligation," Chem. Commun. **49**, 8623–8625 (2013).
31. D. G. Bailey, "Sub-pixel estimation of local extrema," in *Proceeding of Image and Vision Computing New Zealand* (2003), pp. 414–419.
32. E. T. Vandenberg, L. Bertilsson, B. Liedberg, K. Uvdal, R. Erlandsson, H. Elwing, and I. Lundström, "Structure of 3-aminopropyl triethoxy silane on silicon oxide," J. Colloid Interface Sci. **147**, 103–118 (1991).